

AN ANALYTICAL DIFFUSION-EXPANSION MODEL FOR FORBUSH DECREASES CAUSED BY FLUX ROPES

MATEJA DUMBOVIĆ,¹ BERND HEBER,² BOJAN VRŠNAK,³ MANUELA TEMMER,¹ AND ANAMARIJA KIRIN⁴

¹*Institute of Physics, University of Graz, Universitätsplatz 5, A-8010 Graz, Austria*

²*Department of Extraterrestrial Physics, Christian-Albrechts University in Kiel, Liebnitzstrasse 11, 24098, Kiel, Germany*

³*Hvar Observatory, Faculty of Geodesy, University of Zagreb, Kačićeva 26, HR-10000, Zagreb, Croatia*

⁴*Karlovac University of Applied Sciences, Karlovac, Croatia*

Submitted to ApJ

ABSTRACT

We present an analytical diffusion–expansion Forbush decrease (FD) model *ForbMod* which is based on the widely used approach of the initially empty, closed magnetic structure (*i.e.* flux rope) which fills up slowly with particles by perpendicular diffusion. The model is restricted to explain only the depression caused by the magnetic structure of the interplanetary coronal mass ejection (ICME). We use remote CME observations and a 3D reconstruction method (the Graduated Cylindrical Shell method) to constrain initial boundary conditions of the FD model and take into account CME evolutionary properties by incorporating flux rope expansion. Several flux rope expansion modes are considered, which can lead to different FD characteristics. In general, the model is qualitatively in agreement with observations, whereas quantitative agreement depends on the diffusion coefficient and the expansion properties (interplay of the diffusion and the expansion). A case study was performed to explain the FD observed 2014 May 30. The observed FD was fitted quite well by *ForbMod* for all expansion modes using only the diffusion coefficient as a free parameter, where the diffusion parameter was found to correspond to expected range of values. Our study shows that in general the model is able to explain the global properties of FD caused by FR and can thus be used to help understand the underlying physics in case studies.

Keywords: diffusion — methods: analytical — solar-terrestrial relations — Sun: coronal mass ejections (CMEs)

1. INTRODUCTION

Forbush decreases (FDs) are depressions in the galactic cosmic ray (GCR) count-rate observed around the passage of solar wind transients such as interplanetary coronal mass ejections (ICMEs), stream interaction regions (SIRs), and interplanetary shocks (Forbush 1937; Lockwood 1971; Cane 2000; Belov 2009). ICMEs produce the strongest FDs, which often show a two-step profile, one associated with the shock/sheath region and the other with ICME magnetic structure (Barnden 1973; Cane 2000). The two regions were found to be roughly equally effective in GCR modulation and moreover the modulation of the ICME magnetic structure is found to be particularly effective for magnetic clouds (Richardson and Cane 2011). Magnetic clouds are a subset of ICMEs characterised by low proton temperature, low proton beta parameter and most notably by smoothly rotating magnetic field, indicative of a flux rope magnetic structure (Burlaga et al. 1981; Zurbuchen and Richardson 2006; Rouillard 2011), where a flux rope (FR) is a cylindrical plasma structure with magnetic field lines helically winding around the central axis (Lepping et al. 1990).

Generally, solar activity modulates GCRs, which can be described by a Fokker-Planck transport equation of particle random walk in the frame of reference of the small-scale magnetic irregularities (Parker 1965). Based on this so-called *Parker equation* the four physical mechanisms governing the GCR modulation are diffusion, drifts, convection and energy loss (see also *e.g.* Jokipii 1971; Potgieter 2013, and references therein). FDs can be considered as the disturbances in the GCR distribution caused by local variations in one or more transport parameters. However, it is important to separately model FDs corresponding to different solar wind transients. The shock/sheath region is the region of disturbed conditions and highly fluctuating magnetic field ahead of the ICME and is magnetically connected to the ambient interplanetary space (*e.g.* Kilpua et al. 2017, and references therein). Therefore, shock-associated FD can be modelled as *e.g.* propagating diffusive barrier (Wibberenz et al. 1998) or numerically, by solving the Parker equation (*e.g.* Le Roux and Potgieter 1991; Wawrzynczak and Alania 2010; Alania et al. 2013). The ICME magnetic structure is not magnetically connected to the ambient plasma and is characterised by smooth magnetic field (*e.g.* Kilpua et al. 2017, and references therein). Recently, Jordan et al. (2011) revisited the two-step nature of FDs attributing the variety of FD profiles to small-scale interplanetary magnetic field structures, but nevertheless since the two regions are characterised by different properties it is reasonable to regard them as two different global structures with respect to FD modelling, especially given that they are not always encountered together (Richardson and Cane 2011).

It was first proposed by Morrison (1956) that FDs might be clouds of closed magnetised plasma, where they are initially empty of particles and slowly fill as they propagate through the interplanetary space. This approach has been since utilised in several studies to explain FR-associated FDs, where the particles are allowed to enter via “cross-field” transport, *i.e.* perpendicular diffusion (Cane et al. 1995; Munakata et al. 2006; Quenby et al. 2008; Subramanian et al. 2009) and/or drifts (Krittinatham and Ruffolo 2009) and gyration (Kubo and Shimazu 2010). Strictly speaking, the transport across the FR boundary cannot easily be explained by the simple perpendicular (sub)diffusion, because the field lines on opposite sides of the FR boundary are not connected (Jokipii 1966; Ruffolo et al. 2008; Krittinatham and Ruffolo 2009). However, the “cross-field” transport also refers to another mechanism which considers a situation where the particle motion is not bound to its original guiding field line, resulting in diffusion at late times (Ruffolo et al. 2008; Krittinatham and Ruffolo 2009). Furthermore, a change of the magnetic connectivity of the FR can occur due to reconnection allowing magnetic fluctuations (and therefore particles) to diffuse inside FR (Masías-Meza et al. 2016). Krittinatham and Ruffolo (2009) have shown that particles can enter *via* gradient and curvature drifts, however, according to their simulations drift orbits in the FR were spatially restricted to the areas close to the FR boundary and a large fraction exits the FR after several minutes. Similar results were obtained by Kubo and Shimazu (2010) from an analytical model based on gyration. The conclusion in both studies was that diffusion is needed to explain the transport of particles into the interior of the FR. The diffusion approach is generally considered valid when the gyroradius is smaller than the size of the FR (*e.g.* Subramanian et al. 2009), and Blanco et al. (2013) showed that for FRs detected by *Helios* spacecraft typical rigidity of a GCR with gyroradius corresponding to the size of FR is of the order of ~ 100 GV. Therefore, the diffusion approach should be valid to explain FR associated FDs detected in a variety of instruments corresponding to different mean energies: muon telescopes at ~ 50 GV (*e.g.* Kozai et al. 2016), neutron monitors at ~ 10 GV (*e.g.* Clem and Dorman 2000), and spacecraft such as the *Electron Proton Helium Instrument* (EPHIN, Müller-Mellin et al. 1995) onboard *Solar and Heliospheric Observatory* (SOHO, Domingo et al. 1995) at ~ 1 GV (*e.g.* Kühl et al. 2015). The models based on perpendicular diffusion (Cane et al. 1995; Munakata et al. 2006; Quenby et al. 2008; Subramanian et al. 2009) are in a good qualitative agreement with the observation,

reflecting some of the observational characteristics of FDs caused by ejecta such as symmetric shape constrained to the spatial extent of the flux rope and relation of the FD amplitude to the magnetic field strength, the FR size and ICME transit time (Cane 1993; Belov 2009; Dumbović et al. 2011, 2012; Blanco et al. 2013; Badruddin and Kumar 2016; Masías-Meza et al. 2016), although there are evidences that simple diffusion FD models cannot fully explain observations (Richardson and Cane 2011).

In addition to the particle diffusion, another important contribution comes from the expansion of the FR. It was first proposed by Laster et al. (1962) and Singer et al. (1962) that expansion is needed to explain the observational properties of FDs. More recently the diffusion–expansion approach was applied by Munakata et al. (2006) and Kuwabara et al. (2009) in a numerical model best-fitted to the measurements taken by the muon network at Earth (rigidities 50-100 GV) and was utilised to determine the orientation of the interplanetary flux rope. The diffusion–expansion approach was also implemented by Subramanian et al. (2009) and Arunbabu et al. (2013) in an analytical model and was compared to GRAPES-3 muon telescope (rigidities 12-42 GV). These authors estimated the radial perpendicular diffusion coefficient to be of the order of $10^{21} \text{ cm}^2 \text{ s}^{-1}$, however, it should be noted that their studies are adjusted to large events associated with a shock and observed at high particle rigidities. At rigidities of about 1 GV Cane et al. (1995) estimated a diffusion coefficient of about $10^{19} \text{ cm}^2 \text{ s}^{-1}$ utilising spacecraft measurements and less energetic ejecta. Both are roughly in agreement with values obtained from the typical empirical expression used in numerical models (see Equations 23 and 24 in Potgieter 2013). Therefore, these studies outline a rough constraint on the diffusion coefficient used to model FR-associated FD. Since both diffusion and expansion are processes which presumably start close to the Sun, FR *i.e.* CME initial properties need to be considered in the model. This ejecta-only FD model primarily describes FDs associated with ICMEs without shock/sheath region, because shock/sheath region presumably introduces additional decrease *via* different physical mechanisms, but could also be applied to explain the ejecta part of FD in two-step FDs. The aim of this study is to take these considerations into account in the diffusion–expansion model to improve our understanding on the cause, formation, and evolution of FDs.

2. THE BASIC DIFFUSION MODEL

First we consider an analytical FD model based on the perpendicular diffusion of GCRs into the FR, similar to Cane et al. (1995). In this basic diffusion model the FR is regarded as a closed magnetic structure, rooted at the Sun, which is initially empty of GCRs (Figure 1a). The FR is of cylindrical form (hereafter approximated by a long cylinder), it moves with constant velocity and as it moves, it does not vary in shape or size (Figure 1b). We note that the assumption of constant velocity is in general not valid, as it was shown that CMEs slower than the solar wind accelerate, whereas CMEs faster than the solar wind decelerate (*e.g.* Sheeley et al. 1999; Gopalswamy et al. 2000), which is attributed to the magnetohydrodynamical drag (see *e.g.* Vršnak et al. 2013; Hess and Zhang 2014; Sachdeva et al. 2015, and references therein). However, since the acceleration/deceleration depends on the difference between the CME and solar wind speed, for a substantial subset of CMEs (and especially the slower ones which do not drive shocks) constant velocity can be taken as a relatively fair approximation. We also note that the assumption of constant shape and size might not hold true, as it was shown that CMEs expand while propagating in the interplanetary space (*e.g.* Bothmer and Schwenn 1998; Leitner et al. 2007; Janvier et al. 2014) and that their shape might deform during propagation (*e.g.* Cargill et al. 1994; Liu et al. 2006). The deformation of shape is mainly kinematic effect, therefore, the approximation of the constant shape is closely related to the constant velocity approximation. On the other hand, CME expansion is an important feature that may drastically influence the interaction of CMEs and GCRs and will be addressed in the next section.

Furthermore, it is assumed that the GCR density outside the FR is constant and that the GCR can enter the interior of the FR only *via* perpendicular, *i.e.* radial diffusion. It has been shown that there is a radial gradient of GCRs of about $\sim 3\%/AU$ (*e.g.* Webber and Lockwood 1999; Gieseler and Heber 2016; Lawrence et al. 2016). Recently, Marquardt et al. (2018) used Helios E6 data to show that the gradient of the anomalous cosmic ray oxygen is increasing with decreasing distance to Sun. Therefore, the assumption of constant GCR density outside the FR is not entirely correct. However, for simplicity we assume that the change of the outside density of $\sim 3\%$ throughout the evolution of the FR to 1 AU will not notably influence the filling rate of GCRs into the FR and therefore we keep the assumption that the GCR density outside the FR is constant (the estimation to justify this assumption is given at the end of Section 3).

With the assumptions listed above the density of GCRs can be calculated based on the radial diffusion equation for a long cylinder given by *e.g.* Crank (1975):

$$\frac{\partial U}{\partial t} = \frac{1}{r} \left(\frac{\partial}{\partial r} \left(r D_{\perp} \frac{\partial}{\partial r} \right) \right), \quad (1)$$

where $U = U(r, P, t)$ is the GCR phase space density, D_{\perp} is the perpendicular (radial) diffusion coefficient related to GCR rigidity, P (here-forth denoted simply as D), t is time, and r is the radial distance from the FR centre. For particles of specific rigidity $U = U(r, t)$ and the partial differential equation is solved using the method of separation of variables ($U(r, t) = T(t)R(r)$), under the assumption that the diffusion coefficient does not depend on r . The time dependence is then given by the expression (see *e.g.* Crank 1975; Butkov 1968, for details):

$$T(t) = e^{-\lambda^2 D t}, \quad (2)$$

where λ is a constant determined by the initial and boundary conditions. It can be shown that the equation for the radial dependance can be written in a form:

$$r^2 R(r)'' + r R(r)' + \lambda^2 r^2 R(r) = 0, \quad (3)$$

which is the Bessel's equation of the order 0. The solution of Equation 3 can be generally written as a linear combination of the Bessel and Neumann functions, $J_0(\lambda r)$ and $N_0(\lambda r)$, respectively. However, the solution must be finite in the center of the FR, *i.e.* $R(\lambda r)$ finite at $r = 0$, and thus only $J_0(\lambda r)$ is admissible as a solution ($N_0(\lambda r)$ is not finite in $r = 0$, see *e.g.* Butkov 1968, for details). Therefore, the general solution of Equation 1 is:

$$U(r, t) = C J_0(\lambda r) e^{-\lambda^2 D t}, \quad (4)$$

where C and λ are constants determined by the initial and boundary conditions, which can be written in the form:

$$U(r, t) = \begin{cases} 0, & 0 < r < a, t = 0 \\ U_0, & r = a, t \geq 0 \end{cases} \quad (5)$$

a is the radius of the FR and U_0 is the GCR phase space density at its surface. With these initial and boundary conditions, the solution for the particle density inside the flux rope can be written (see Equation 5.22 in Crank 1975):

$$U(r, t) = U_0 \left(1 - \frac{2}{a} \sum_{n=1}^{\infty} \frac{J_0(\lambda_n r)}{\lambda_n J_1(\lambda_n a)} e^{-D \lambda_n^2 t} \right), \quad (6)$$

where J_0 and J_1 are Bessel functions (of the first kind) of the order 0 and 1, respectively, and λ_n are defined by the positive roots of $J_0(\lambda_n a) = 0$ ($\lambda_n = \frac{\alpha_n}{a}$, α_n are positive roots of J_0), which are tabulated in tables of Bessel functions. Bessel functions J_0 have oscillatory character whereas the exponential function rapidly decreases with α_n^2 , therefore the solution can be approximated as:

$$U(r, t) = U_0 \left(1 - C \frac{2}{\alpha_1} \frac{J_0(\alpha_1 \frac{r}{a})}{J_1(\alpha_1)} e^{-D (\frac{\alpha_1}{a})^2 t} \right), \quad (7)$$

where the constant C depends on the initial and boundary conditions defined in Equation 5. The final solution is then given by the expression:

$$U(r, t) = U_0 \left(1 - J_0(\alpha_1 \frac{r}{a}) e^{-D (\frac{\alpha_1}{a})^2 t} \right). \quad (8)$$

The corresponding Forbush decrease can be represented by $A(\%) = (U(r, t)/U_0 - 1) \cdot 100\%$, where the radial dependence for a given diffusion time depicts its shape and magnitude at a certain location in the heliosphere.

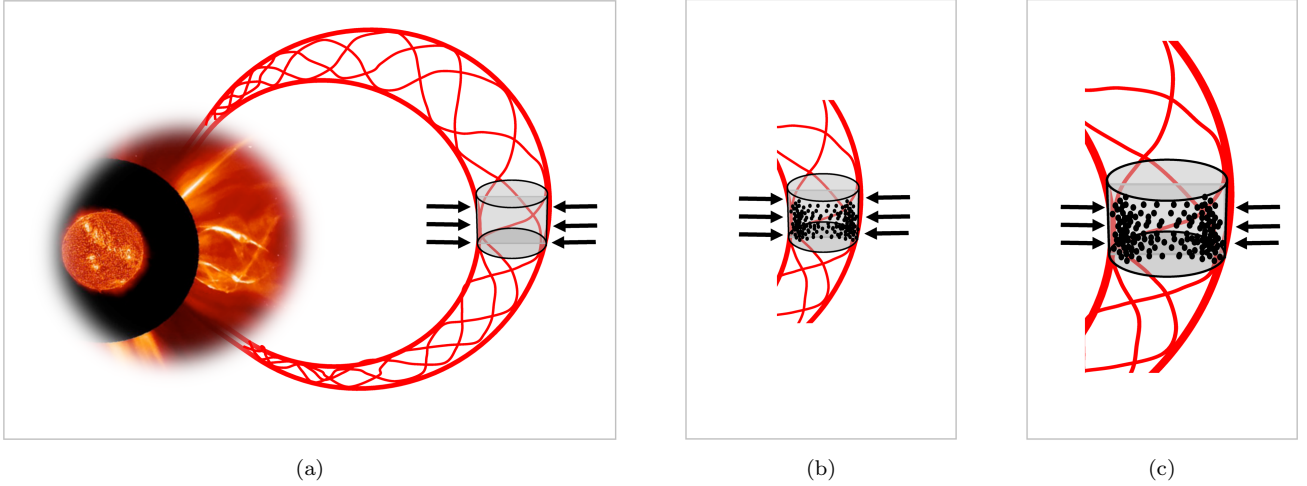


Figure 1. a) A sketch of the initial FR for both diffusion-only and diffusion-expansion model: FR is a closed magnetic structure locally of the cylindrical form, rooted at the Sun and initially empty of GCRs; b) A sketch of the diffusion-only model after time t : FR does not vary in shape or size; c) A sketch of the diffusion-expansion model after time t : FR expands self-similarly. In both cases particles enter the FR by perpendicular diffusion. Image of the Sun is adapted from the remote EUV and coronagraphic observations by *SOHO*.

3. THE DIFFUSION-EXPANSION MODEL

Now we introduce the expansion of the FR by allowing that the radius changes with time (Figure 1c). We note that we do not take into account the energy-loss effect (adiabatic cooling) due to FR expansion. In general, the energy-loss is expected to introduce additional modulation effects (see *e.g.* Lockwood 1971, and references therein), but the quantitative contribution is not trivial to estimate. The energy-loss term is proportional to $\partial U / \partial \ln P$ and to some extent balances out the inward diffusion of particles (Munakata et al. 2006). Therefore, it is reasonable to expect that neglecting the GCR energy loss could result in a somewhat underestimated FD amplitudes.

Furthermore, we allow the diffusion coefficient to change with time as well, since it presumably depends on the magnetic field strength (Potgieter 2013), which in general also changes in time (*e.g.* Démoulin et al. 2008). Consequently, the dependence on the radial distance and time are not independent and the method of separation of variables is no longer applicable to Equation 1. However, with the substitution $r(t) \rightarrow \hat{r}(t)/a(t)$ Equation 1 can be rewritten in a form:

$$\frac{\partial U}{\partial t} = \frac{D(t)}{a(t)^2} \frac{1}{\hat{r}} \left(\frac{\partial}{\partial \hat{r}} \left(\hat{r} \frac{\partial}{\partial \hat{r}} U \right) \right), \quad (9)$$

where \hat{r} is the normalized radial distance, scaled to the radius of the flux rope ($\hat{r} = r(t)/a(t)$), whereas $D(t)$ and $a(t)$ are time-dependent diffusion coefficient and flux rope radius, respectively. With the assumption that the ratio $r(t)/a(t)$ does not change with time (which is discussed below), the method of separation of variables can be applied to Equation 9. The form of the radial solution remains the same, whereas the time-dependent solution can be written in the form:

$$T(t) = e^{-\lambda^2 \int \frac{D(t)}{a(t)^2} dt}. \quad (10)$$

Note that the initial and boundary conditions need to be rewritten accordingly:

$$U(\hat{r}, t) = \begin{cases} 0, & 0 < \hat{r} < 1, t = 0 \\ U_0, & \hat{r} = 1, t \geq 0 \end{cases} \quad (11)$$

Following the same procedure as described in Section 2 the final solution can be written as:

$$U(\hat{r}, t) = U_0 \left(1 - J_0(\alpha_1 \hat{r}) e^{-\alpha_1^2 f(t)} \right), \quad (12)$$

where U_0 is the GCR phase space density at the FR surface, J_0 is a Bessel function (of the first kind) of the order 0, α_1 is a first positive root of J_0 (tabulated in tables of Bessel functions), \hat{r} is the radial distance scaled to the FR radius ($\hat{r} = r(t)/a(t)$), and $f(t)$ is a function of time that depends on the interplay between the diffusion of GCR into the FR and its expansion. Since $f(t)$ depends on the ratio $D(t)/a(t)^2$, where both $D(t)$ and $a(t)$ are generally not known and are still subject of ongoing studies, it is a somewhat arbitrary function. However, there are some basic constraints on the function $f(t)$. Firstly, it must not diverge at $t = 0$ and moreover, due to the initial condition, it must satisfy $f(t = 0) = 0$. Secondly, the behaviour of the function is constrained by observations. Cane et al. (1994) and Blanco et al. (2013) found that the FD amplitude decreases with heliospheric distance, indicating that the GCR density within the FR increases with time. Therefore, we expect $f(t)$ to be a positive and monotonically increasing function. Further constraints on the function $f(t)$, *i.e.* the solution given in Equation 12, can be achieved through comparison of the model results with observations, while a general behaviour is derived in the continuation of this Section based on empirical FR relations.

In Equation 9 we assumed that the ratio $r(t)/a(t)$ does not change with time in order to apply the method of separation of variables. This assumption holds when the change rate of any shell within the cylinder is proportional to the change rate of its outermost shell, $dr/da = \text{const.}$, *i.e.* when $r(t) = \text{const} \cdot a(t)$. It can be easily shown that this holds when the cylinder is expanding self-similarly, *i.e.* in a way that at later times it is a scaled reproduction of its original shape. This means that the coordinates of a plasma element at a given time are scaled by a time-dependent factor compared to the reference-time value t_0 , $x_i(t) = x_i(t_0)f_i(t)$, where x_i is the plasma coordinate and $f_i(t)$ a corresponding time-dependant factor in the i direction (Démoulin et al. 2008). Therefore, a self-similar expansion of a FR radius can be written as:

$$a(t) = a_0 \left(\frac{R(t)}{R_0} \right)^{n_a}, \quad (13)$$

where $R(t)$ is the heliospheric distance at time t , R_0 is the starting heliospheric distance, a_0 is the starting FR radius and n_a is the power-law index which observational studies approximately constrain to $0.45 < n_a < 1.14$ (see *e.g.* Bothmer and Schwenn 1998; Leitner et al. 2007; Démoulin et al. 2008; Gulisano et al. 2012). An expression similar to Equation 13 can be used to describe the corresponding decrease of the central magnetic field:

$$B(t) = B_0 \left(\frac{R(t)}{R_0} \right)^{-n_B}, \quad (14)$$

where B_0 is the initial magnetic field and n_B is the power-law index which observational studies approximately constrain to $0.88 < n_B < 1.89$ (*e.g.* Gulisano et al. 2012, and references therein). Using Equations 13 and 14 we can consider different types of FR expansion based on the axial magnetic flux. The axial magnetic flux is given as $\Phi_{ax} = B_\phi S$, where B_ϕ is the axial magnetic field, which is in a force free FR model related to the magnetic field in the FR center, B_c (*e.g.* Lundquist 1951), and S is the cross section of the FR. Assuming a circular cross section the axial magnetic flux is given by $\Phi_{ax} \sim B_c a^2$, which can be used to determine the power-law index in Equation 14 with the assumption that the magnetic flux is conserved ($n_B = 2n_a$). However, observational studies involving n_B and n_a measurements have shown that n_B is not necessarily equal to $2n_a$ (see Gulisano et al. 2012, and references therein). For instance, Gulisano et al. (2010) report $n_a = 0.89$ and $n_B = 1.85$ for non-perturbed magnetic clouds (those showing pronounced linear velocity profile), *i.e.* $n_B \approx 2n_a$. However, for the perturbed magnetic clouds they found that they expand less with distance, with $n_a = 0.45$ and $n_B = 1.89$, *i.e.* $n_B - 2n_a > 0$. On the other hand, Leitner et al. (2007) found that magnetic clouds in general show $n_a = 1.14$ and $n_B = 1.64$, *i.e.* $n_B - 2n_a < 0$. Mentioned studies are focused on the inner solar system between 0.3 and 1 AU, which is the main focus of this study as well, therefore, based on these observational studies we consider three different expansion trends: $n_B - 2n_a = 0$, $n_B - 2n_a > 0$, and $n_B - 2n_a < 0$. Physically, these expansion trends relate $n_B - 2n_a = 0$ to the magnetic flux conservation, $n_B - 2n_a > 0$ to a decrease of the magnetic flux with heliospheric distance, whereas $n_B - 2n_a < 0$ is related to the increase of the magnetic flux.

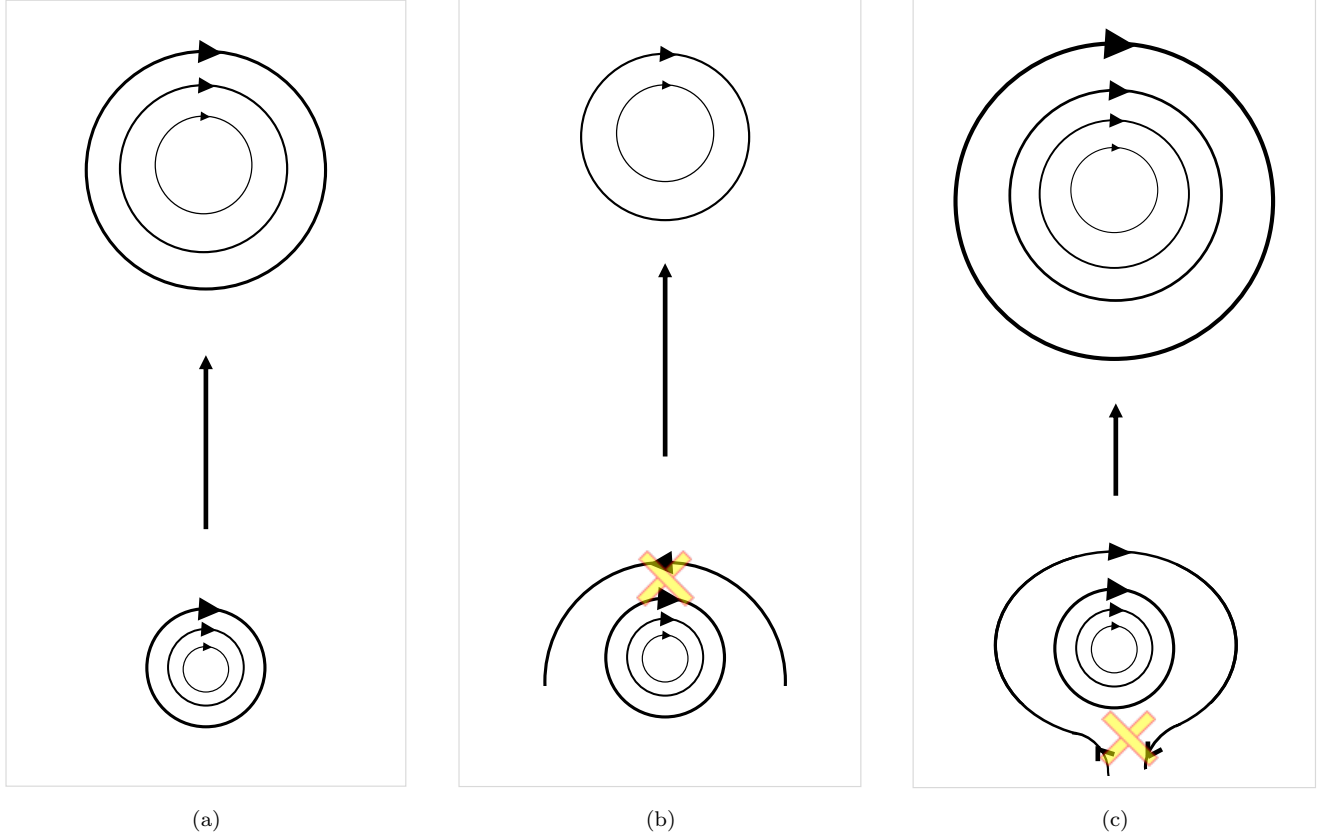


Figure 2. A sketch of three different FR expansion trends: a) relative increase in the FR cross-sectional area is “balanced” by the decrease in the strength of the central magnetic field (magnetic flux conserved); b) increase in the FR cross-sectional area is relatively slow compared to the decrease in the strength of the central magnetic field (magnetic flux decreased); c) increase in the FR cross-sectional area is relatively fast compared to the decrease in the strength of the central magnetic field (magnetic flux increased). View of the FR cross section is shown with field lines in poloidal direction. The yellow cross marks the point of reconnection (interaction with the ambient plasma).

Observational evidence for the reduction of the magnetic flux through erosion due to magnetic reconnection was found in studies by *e.g.* Dasso et al. (2007) and Ruffenach et al. (2015), whereas Manchester et al. (2014) suggest that the reconnection at the rear of the flux rope can lead to flux injection (for an overview of various processes affecting the axial magnetic flux evolution see Manchester et al. 2017). We note that the interaction of the FR with the ambient plasma affects the ordered structure of the FR in the outer FR layers, but from the aspect of the model we are only concerned about the relative increase of the FR cross-sectional area compared to the decrease of the central magnetic field strength. This is visualised by three corresponding sketches in Figure 2.

Based on these considerations on the FR expansion we can determine the function $f(t) = \int D(t)/a(t)^2 dt$, which defines the time dependent part of the solution given in Equation 12. We assume that the FR moves with a constant velocity $v = R/t$ and that the change of the FR radius and of the central magnetic field is given by Equations 13 and 14, respectively. Furthermore, we assume that the diffusion coefficient relates to the magnetic field strength $D \sim 1/B$ (see *e.g.* Potgieter 2013, and references therein) and therefore increases with heliospheric distance with a power-law index n_B . With these assumptions the time dependent part is reduced to:

$$f(t) = \frac{D_0}{a_0^2} \cdot \left(\frac{v}{R_0}\right)^x \cdot \int t^x dt, \quad (15)$$

where $x = n_B - 2n_a$. In the case of the conserved magnetic flux $x = 0$ and integration is trivial. In cases where the flux is not conserved we consider simple options where $x = 0.5$ and $x = -0.5$ for decreased and increased flux, respectively. The selected options are simple to integrate and are related to the n_B and n_a ranges restricted by the

above mentioned observational studies. For both $x = 0.5$ and $x = -0.5$ integration results in rational functions, as well as for any other value of x , except for $x = -1$ when integration of $f(t) \sim \int t^x dt$ results in a logarithmic function. Therefore, $x = -1$ is considered as a fourth, special case of expansion. We note that reconnection would change the magnetic connectivity of the FR allowing additional GCRs to stream in (Masías-Meza et al. 2016). Therefore, it is reasonable to expect that the diffusion coefficient would be influenced to some extent. On the other hand, since $f(t)$ and x -values we use in the model are arbitrarily selected (although empirically based), for the sake of simplicity, we do not include this effect in our calculations.

To summarise, we consider the solution of the diffusion-expansion equation given in Equation 12 for four different types of expansion which lead to four different types of $f(t)$ governing the time-behaviour of the modelled FD:

1. $n_B - 2n_a = 0, x = 0 \longrightarrow f(t) \propto t$ (conserved magnetic flux)
2. $n_B - 2n_a > 0, x = 0.5 \longrightarrow f(t) \propto t^{\frac{3}{2}}$ (reduced magnetic flux)
3. $n_B - 2n_a < 0, x = -0.5 \longrightarrow f(t) \propto t^{\frac{1}{2}}$ (increased magnetic flux)
4. $n_B - 2n_a < 0, x = -1 \longrightarrow f(t) \propto \ln(at + 1)$ (increased magnetic flux - special case)

We note that initial CME parameters, which are needed to quantify the solution of Equation 15 (a_0 , v , and R_0), can be obtained from remote CME observation using *e.g.* 3D CME reconstruction. On the other hand, D_0 is unknown and cannot be obtained from remote observation, therefore it has to be estimated. For that purpose we estimate the diffusion coefficient near Earth, D_E (following the typical empirical expression used in numerical models, see Potgieter 2013) and back-extrapolate to $R_0 = 20 R_\odot$ using assumed power-law behaviour. Namely, we assume $D \sim 1/B$, B following the power-law given in Equation 14, where $n_B = 2$ for expansion types $x = 0$ and $x = 0.5$, and $n_B = 1$ for expansion types $x = -0.5$ and $x = -1$. Given that $x = n_B - 2n_a$, this implicitly defines the power-law index given in Equation 13, where $n_a = 1$ for expansion type $x = 0$, $n_a = 0.75$ for $x = 0.5$, $n_a = 0.75$ for $x = -0.5$, and $n_a = 1$ for $x = -1$.

In Figure 3 the solutions of the model for different types of expansion, diffusion coefficients, transit times and FR radius are presented. Figures 3a and b show relative GCR phase space density as a function of the radial position within the FR after a transit time of 84 h for two different values of the initial diffusion coefficient, D_0 , respectively. Different D_0 were estimated as described above based on the diffusion coefficients at Earth, D_E , which roughly correspond to values obtained from Equations 23 and 24 by Potgieter (2013) for 1 GV GCRs in a 10 and 30 nT magnetic field. A generic CME was used, having the initial radius $a_0 = 5 R_\odot$ at a distance $R_0 = 20 R_\odot$, and arriving at Earth after a transit time of $t = 84$ h (*i.e.* moving at a constant speed of $\approx 500 \text{ km s}^{-1}$). The dashed magenta line marks the center of FR, defining the relative FD magnitude, A_m . The five curves correspond to different types of expansion: no expansion (diffusion only approach with constant size, as described in Section 2) and four different types of expansion described above. In the case of no expansion the radius of the generic CME is constant and has a value $a = 0.1$ AU, and the diffusion coefficient is also constant with a value corresponding to D_E . Figures 3c and d show the time evolution of the FD magnitude, A_m , for two different values of D_0 used in Figures 3a and b, respectively. Also the same generic CME and different expansion types are applied as in Figures 3a and b. Two selected transit times are highlighted by dashed magenta lines. Figures 3e and f show the FD magnitude at Earth, A_m , *vs* the diffusion coefficient at Earth, D_E , for a generic CME ($a_0 = 5 R_\odot$, $R_0 = 20 R_\odot$) moving at a speed of ≈ 1150 and $\approx 500 \text{ km s}^{-1}$, respectively (corresponding to the transit times to Earth of 36 and 84 h, respectively). Different expansion types are applied as in Figures 3a-d. Two selected D_E (used in Figures 3a and b) are highlighted by dashed magenta lines. Finally, Figures 3g and h show the FD magnitude, A_m , after a transit time of 84 h *vs* the initial FR radius for two different values of D_0 used in Figures 3a and b, respectively. Two selected initial FR radii ($a_0 = 0.5 R_\odot$ and 0.1 AU used in Figures 3a and b for different expansion types and no expansion, respectively) are highlighted by dashed magenta lines (for no expansion case initial FR radius equals the one at Earth because $a = \text{const.}$).

It can be seen in Figures 3a and b that the relative GCR phase space density has a symmetric shape within the FR, reaching its minimum in the center of the FR and is restricted to the FR extent. The shape is qualitatively the same regardless of the expansion type and diffusion coefficient and shows a qualitative agreement with observed ejecta-FD profiles (*e.g.* Cane 1993; Belov et al. 2015; Masías-Meza et al. 2016). Furthermore, we note that qualitatively, for all expansion cases, A_m decreases with time as can be seen in Figures 3c and d, which is also in agreement with observational studies (Cane et al. 1994; Blanco et al. 2013). Quantitatively, it can be seen in Figures 3a and b that

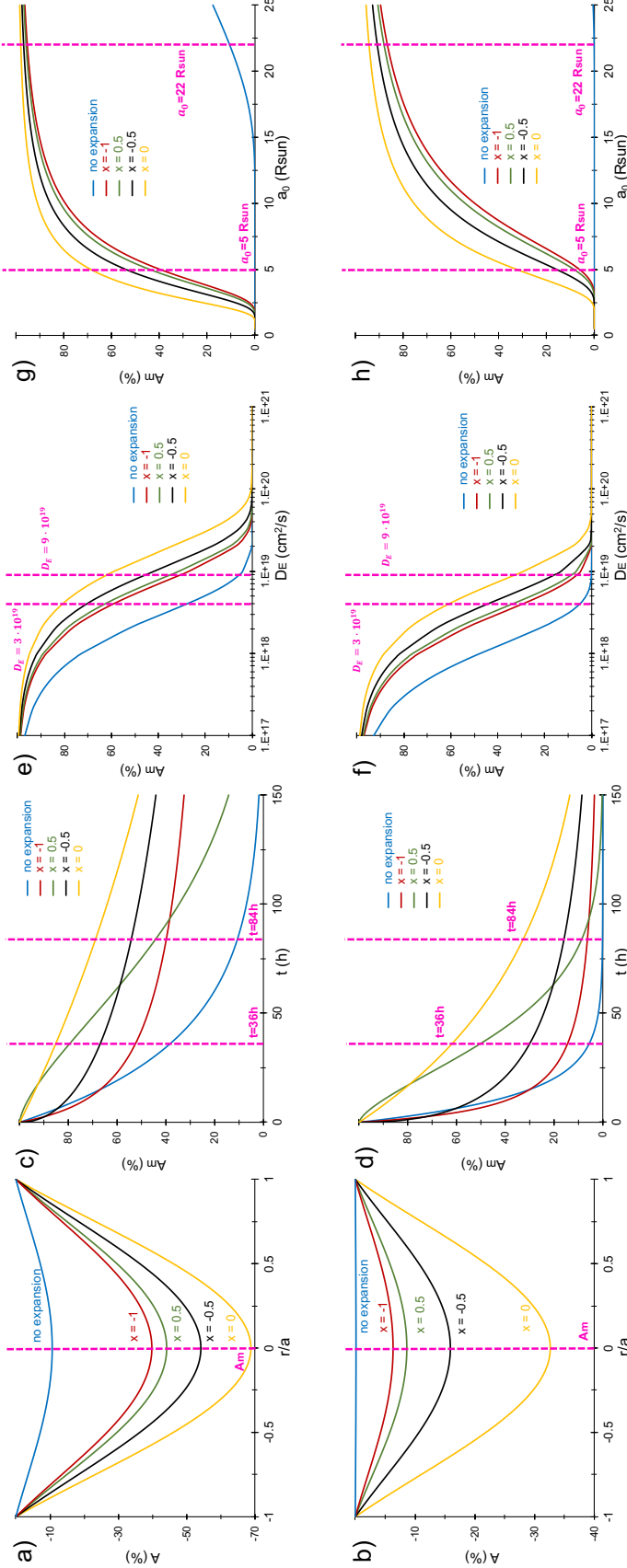


Figure 3. a) The relative GCR phase space density, A , as a function of the radial position within the FR, r/a , after a transit time of 84 h for different types of expansion of a generic CME ($a_0 = 5 R_\odot$, $R_0 = 20 R_\odot$, $v \approx 500 \text{ km s}^{-1}$) and no expansion case ($a = 0.1 \text{ AU}$, $D_0 = D_E$) for $D_E = 3 \times 10^{18} \text{ cm}^2 \text{ s}^{-1}$ ($D_0 = 2.6 \times 10^{16} \text{ cm}^2 \text{ s}^{-1}$ for $x = 0$ and $x = 0.5$; $D_0 = 2.8 \times 10^{17} \text{ cm}^2 \text{ s}^{-1}$ for $x = -0.5$ and $x = -1$). The dashed magenta line marks the position of the FR center where the relative FD magnitude, A_m , is defined.
b) Same as in a) for $D_E = 9 \times 10^{18} \text{ cm}^2 \text{ s}^{-1}$ ($D_0 = 7.7 \times 10^{16} \text{ cm}^2 \text{ s}^{-1}$ for $x = 0$ and $x = 0.5$; $D_0 = 8.4 \times 10^{17} \text{ cm}^2 \text{ s}^{-1}$ for $x = -0.5$ and $x = -1$).
c) Time evolution of the FD magnitude, A_m , for $D_E = 3 \times 10^{18} \text{ cm}^2 \text{ s}^{-1}$. The same generic CME and different expansion types are applied as in a) and b). Two selected transit times are highlighted by dashed magenta lines.
d) Same as in c) for $D_E = 9 \times 10^{18} \text{ cm}^2 \text{ s}^{-1}$.
e) FD magnitude at Earth, A_m , vs diffusion coefficient at Earth, D_E , for a generic CME ($a_0 = 5 R_\odot$, $R_0 = 20 R_\odot$) moving at a speed of $\approx 1150 \text{ km s}^{-1}$ (transit time 36 h). Different expansion types are applied as in a)-d). Two selected D_E are highlighted by dashed magenta lines.
f) Same as in e) for $v = 500 \text{ km s}^{-1}$ (transit time 84 h).
g) FD magnitude, A_m , after a transit time of 84 h vs the initial FR radius, a_0 , for $D_E = 3 \times 10^{18} \text{ cm}^2 \text{ s}^{-1}$ and different expansion types as in a) and b). Two selected a_0 are highlighted by dashed magenta lines.
h) Same as in g) for $D_E = 9 \times 10^{18} \text{ cm}^2 \text{ s}^{-1}$.

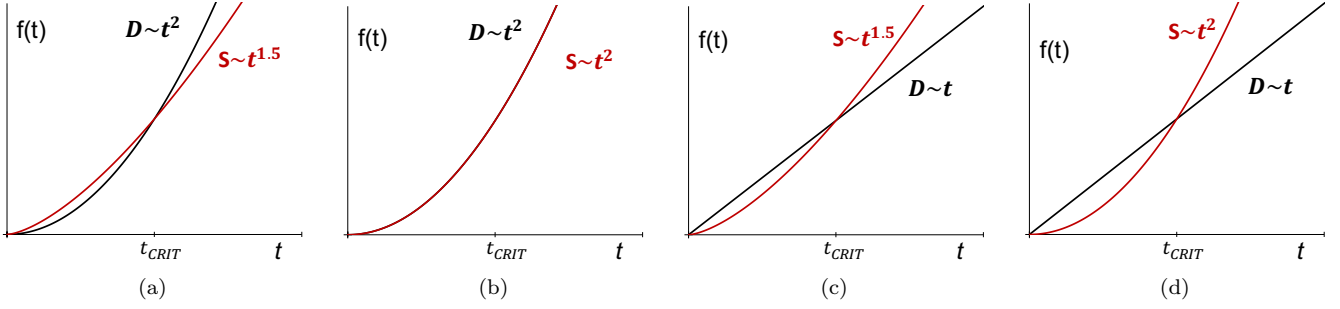


Figure 4. Time dependencies of diffusion coefficient, D , and cross-sectional area, S , for different expansion types: a) $x = 0.5$ (magnetic flux decreased); b) $x = 0$ (magnetic flux conserved); c) $x = -0.5$ (magnetic flux increased); d) $x = -1$ (magnetic flux increased - special case). D , S , and t are given in arbitrary units. t_{CRIT} marks the point between small and large t -regimes.

the amplitude of the depression depends on both diffusion coefficient and expansion type. The relative amplitude of the GCR phase space density in the FR center, *i.e.* the FD magnitude, A_m , is smaller for larger diffusion coefficient at Earth, D_E , which is also evident from Figures 3e and f. This reflects the fact that larger D_E means more efficient diffusion of GCRs into the FR, *i.e.* faster filling up. Therefore, for the same diffusion time and a_0 , FR with larger D_E will have more GCRs, *i.e.* smaller A_m than the FR with smaller D_E .

The relation to the expansion type is not so simple. Comparing Figures 3a and b one might get the impression that A_m is smallest for the no expansion case and largest for the $x = 0$ expansion type. However, Figures 3c and d reveal that this depends strongly on the transit time after which A_m is observed. In general, we expect that A_m depends on a complex interplay of diffusion and expansion as given by Equation 15. However, it should be noted that these two effects are not independent of each other. On one hand, the expansion increases the diffusion coefficient (as B decreases) enhancing the diffusion, while on the other hand, increases the FR size and therefore acts as a “diluting” mechanism (see Figures 3g and h). We also note that the initial diffusion coefficients D_0 are not the same for all expansion types, due to the fact that we fix the diffusion coefficient at Earth D_E and back-extrapolate it using different power-laws. Finally, the functional character of the solutions obtained from Equation 15 needs to be taken into account. This is shown in Figure 4, where for different expansion types the time-dependencies of diffusion coefficient, D , and cross-sectional area, S , are shown (in arbitrary units).

It can be seen in Figure 4 that the expansion can both enhance and slow down the diffusion for different expansion types, depending on the time regime, which is defined according to t_{CRIT} (determined by the values of D , S , and t).

Namely, in the small t -regime, $t < t_{CRIT}$, the following is observed for different expansion types:

- for $x > 0$ the increase of S is faster than the increase of $D \rightarrow$ the expansion slows down the diffusion
- for $x = 0$ the increase of S is balanced with the increase of $D \rightarrow$ the expansion does not affect the diffusion
- for $x < 0$ the increase of S is slower than the increase of $D \rightarrow$ the expansion enhances the diffusion

Conversely, in the large t -regime, $t > t_{CRIT}$, we observe the following for different expansion types:

- for $x > 0$ the increase of S is slower than the increase of $D \rightarrow$ the expansion enhances the diffusion
- for $x = 0$ the increase of S is again balanced with the increase of $D \rightarrow$ the expansion does not affect the diffusion
- for $x < 0$ the increase of S is faster than the increase of $D \rightarrow$ the expansion slows down the diffusion

Therefore, in different transit time regimes, different expansion types show different filling efficiency. This results in complex trends of the $A_m(t)$ curves for different expansion types, which cross each other on several occasions (see Figure 3c and d). For example, at very small transit times ($t < 3h$ in Figure 3c) the largest A_m is for $x = 0.5$ (magnetic flux reduced), whereas the smallest A_m is for $x = -1$ (magnetic flux increased-special case). At larger transit times ($t > 18h$ in Figure 3c) the largest A_m is for $x = 0$ (magnetic flux conserved), whereas the smallest A_m is for no expansion case. We note that after some critical transit time (determined by initial conditions) the case of no expansion has smaller A_m than any expansion type. This is not surprising as for no expansion case a constant size

assumption is used. For all expansion cases and for small t , FRs are relatively small compared to the no expansion case and thus easier to fill according to Figures 3g and h. At later stages, where the size of expanding FRs is comparable to the constant size FR, as there is no mechanism to counteract diffusion for no expansion case, the FR fills up more quickly resulting in a smaller A_m .

In conclusion, at a given heliocentric distance, *i.e.* after a specific transit time, A_m will be determined by a complex interplay of the diffusion and expansion depending on the initial conditions (a_0 , D_0), as well as on the expansion type (*i.e.* competing between the drop of B and the increase of S).

Finally, we estimate how much the assumption that the GCR density outside the FR is constant, $U_0 = \text{const.}$, influences our result. For that purpose we use the generic CME from Figure 3d and we assume that U_0 changes by 3% throughout the evolution of the FR to 1 AU (within 84 h transit time), *i.e.* 0.04% per hour. We divide the FD amplitude evolution into 10 quasi-stationary time steps (each time-step lasts for 8.4 h), where between each time-step U_0 increases by $\approx 0.3\%$. We assume that the increase of U_0 leads to a larger difference between FD amplitudes in two consecutive time-steps by factor α : $\Delta A_{\text{new},n} = \alpha \cdot \Delta A_{\text{old},n}$, where $\Delta A_{\text{old},n} = A_{\text{old},n} - A_{\text{old},n+1}$ and $\alpha = 1 + 0.3/100 = 1.003$ (“new” and “old” correspond to $U_0 \neq \text{const.}$ and $U_0 = \text{const.}$, respectively). Here, the values of A_{old} was calculated based on Figure 3d, whereas A_{new} is calculated as $A_{\text{new},n+1} = A_{\text{new},n} - \Delta A_{\text{new},n}$ (in the first time step $A_{\text{old},0} = A_{\text{new},0} = 1$). This procedure reflects the fact that in each time step there are more particles available to enter the FR compared to $U_0 = \text{const.}$ case, but only a fraction of them actually enters the FR in the given time step. With this procedure we estimate a decrease in FD amplitude of 0.2–0.3% (depending on the expansion type) for a 3% increase of U_0 in a transit time of 84 h. This FD decrease corresponds to $< 5\%$ relative uncertainty for the generic CME in Figure 3, which is reasonably low to be neglected. For higher values of the radial gradient, *e.g.*, increase of U_0 of 10%/AU, the estimated change in the FD amplitude is $\approx 1\%$, corresponding to $\sim 15\%$ relative uncertainty, too high to be neglected. However, we note that for the ~ 1 GV protons, which are the main contributors to the observed FD in spacecraft, we expect the radial gradient to be $\sim 3\%$ (Gieseler and Heber 2016), thus we expect the $U_0 = \text{const.}$ assumption to hold.

Furthermore, we can apply the same procedure to estimate whether or not the model could be used to simulate the ejecta part during two-step FDs by assuming that the presence of shock/sheath can be introduced as the variation of U_0 , where U_0 due to the reduced CR count rate in the sheath is $\approx 5\%$ lower after 84 h (based on the typical shock/sheath associated FD amplitude determined by Richardson and Cane 2011). We assume that the decrease in U_0 leads to a smaller difference between FD amplitudes in two consecutive time-steps by factor $\alpha = 1 - 0.05/100 = 0.995$. With this procedure we estimate that a 5% decrease of U_0 in a transit time of 84 h would lead to a decrease in FD amplitude of $< 0.5\%$ for all expansion types, corresponding to $< 8\%$ relative uncertainty for the generic CME in Figure 3, which is still reasonably low. It should be noted, when the sheath region, *i.e.* the standoff distance between CME and shock, increases with the radial distance, the variation of U_0 could depend much stronger on the radial distance than we assumed. In this case the variation rate of U_0 is much smaller than $\approx 5\%/AU$ at smaller radial distances and thus our estimation based on a constant variation rate can be regarded as an upper limit. We also note that in most ICMEs observed at Earth the shock/sheath part of FD amplitudes is $A_{\text{shock}} \leq 5\%$ (Richardson and Cane 2011). Therefore, based on our estimation, we conclude that for a large subset of CMEs the model could also be applied to explain the ejecta part in the case of the two-step FD.

4. CASE STUDY: 2014 MAY 25 CME AND 2014 MAY 30 FORBUSH DECREASE

We select a near-Earth event of 2014 May 30, where an ejecta-only FD was recorded in the interplanetary space by *SOHO*/EPHIN F-detector, which is suitable to detect ejecta-only FDs (see *e.g.* Heber et al. 2015). The event was associated with a magnetic cloud (MC) observed in the *in situ* measurements of the *Magnetic Field Instrument* (MFI, Lepping et al. 1995) and *Solar Wind Experiment* (SWE, Ogilvie et al. 1995) onboard *Wind* spacecraft (Figure 5a). The start/end of the MC is determined based on the drop in temperature and increase of the magnetic field strength, resulting in depressed plasma beta. In addition, throughout thus selected MC borders, signatures of the magnetic field rotation and smoothness are observed (first two panels of Figure 5a). The measured relative FD amplitude is $A = (3.3 \pm 0.1)\%$, where A is the difference between FD minimum and “quiet” time value derived as an average of the “quiet” time measurements in a time period 1.5 days prior to the decrease. The standard error of 0.1 is also estimated based on the “quiet” time *SOHO*/EPHIN measurements.

In order to obtain CME initial parameters to run the FD model described in Section 3 (hereafter *ForbMod*), the ICME recorded *in situ* needs to be associated to a CME observed remotely by coronagraphs. We make a rough estimate of the possible ICME transit time ($TT = 5$ days) based on the plasma speed at the leading edge ($v \approx 350 \text{ km s}^{-1}$)

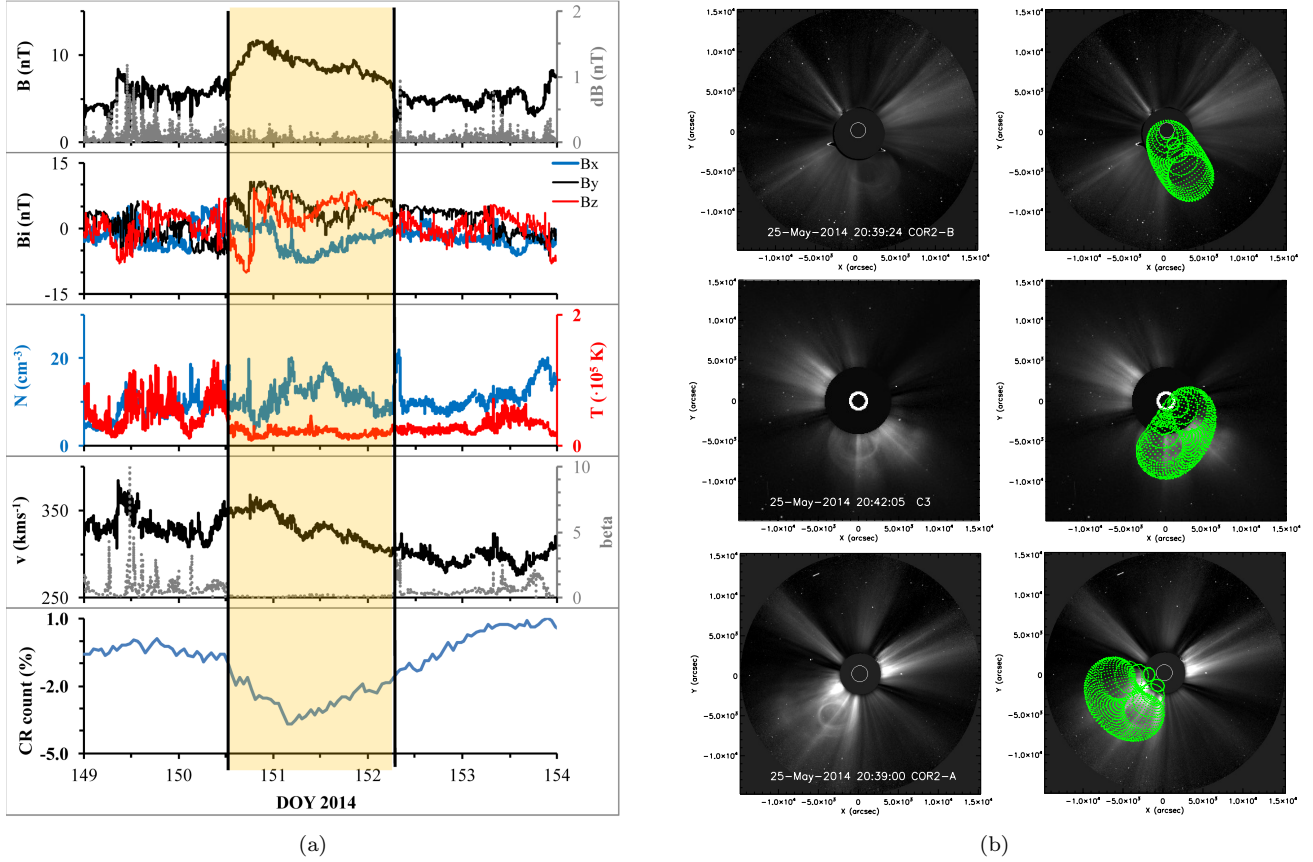


Figure 5. a) *In situ* measurements of the magnetic cloud (1-minute averages) and the corresponding Forbush decrease of 2014 May 30. Top to bottom the panels show: 1) magnetic field strength (black) and fluctuations (gray); 2) magnetic field components (in Geocentric Solar Magnetospheric system); 3) plasma density (blue) and temperature (red); 4) plasma speed (black) and plasma-beta (gray); 5) relative hourly cosmic ray count by *SOHO*/EPHIN.

b) GCS reconstruction for 2014 May 25 CME at 20:39 using coronagraphic images from *STEREO-B*/COR2 (top), *SOHO*/C3 (middle), and *STEREO-A*/COR2 (bottom). Best fit parameters are: longitude (Stonyhurst) = 6°, latitude = -20°, tilt = 57°, height = 18.2 R_{\odot} , aspect ratio = 0.25, and half angle = 15°.

assuming constant speed and search for CMEs within a time window of roughly ± 1 day. The CME should be Earth-directed, therefore, we expect to see a halo or partial halo CME in the *Large Angle Spectroscopic Coronagraph* (LASCO, Brueckner et al. 1995) or a CME with low-coronal signatures relatively close to the center of the solar disc, as seen in the EUV imagers. Using the *SOHO*/LASCO CME Catalog¹ we identified the most likely CME, a very slow partial halo first detected 2014 May 25 at 10:00 UT by LASCO/C2 moving throughout LASCO/C3 field of view until early May 26. We do not observe any obvious on-disc low-coronal signatures in *Atmospheric Imaging Assembly* (AIA, Lemen et al. 2012) EUV imagers onboard *Solar Dynamics Observatory* (SDO) or in EUV imagers onboard *Solar-Terrestrial Relations Observatory* spacecraft (STEREO, Kaiser et al. 2008). *STEREO*/COR1 CME Catalog² reports a faint flux-rope type eruption at 08:00 UT moving south in *STEREO-B* and south-east in *STEREO-A*.

In order to determine the CME initial parameters we use the Graduated cylindrical shell (GCS) model (Thernisien et al. 2006, 2009; Thernisien 2011) which is used to reconstruct the FR structure of the CME using coronagraphic images from different vantage points. The FR is modelled as a self-similarly expanding hollow croissant with origin in the center of the Sun, conical legs, circular cross section and pseudo-circular front. The reconstruction is done by visual comparison of the coronagraphic images from three different vantage points and the modelled FR. At 20:39 UT the CME is seen in *STEREO-A*/COR2, *STEREO-B*/COR2, and *SOHO*/C3, where especially prominent circular-

¹ <https://cdaw.gsfc.nasa.gov/CMElist/>

² <https://cor1.gsfc.nasa.gov/catalog/>

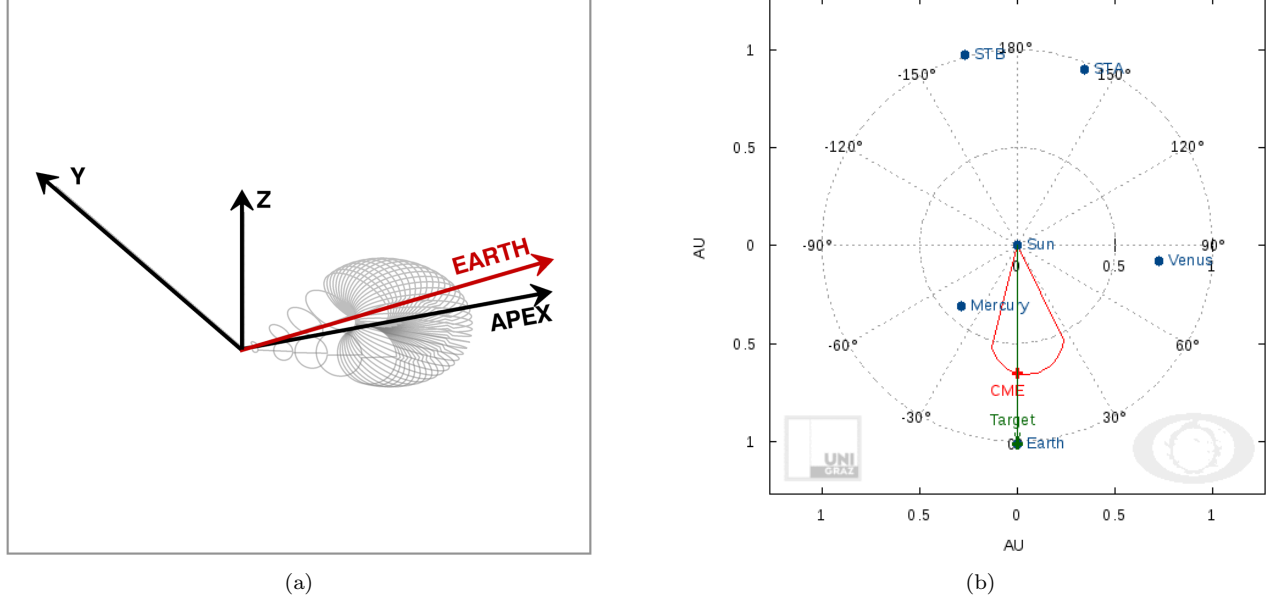


Figure 6. a) 3D plot of the reconstructed flux rope and the relative directions of the CME apex (black) and Earth (red) in the Heliocentric Earth Equatorial (HEEQ) system (Earth direction is along x-axis); b) CME geometry plot in the equatorial plane based on DBM (taken from <http://swe.ssa.esa.int>).

shaped substructure is seen in all three spacecraft (Figure 5b). This prominent feature is thus used as an additional constraint to the GCS (along with the shape of the front), compensating for the fact that the origin of the CME is unknown (no low-coronal on-disc signatures). The best fit is obtained by changing three geometric and three positional parameters. The positional parameters are latitude, longitude and tilt, whereas geometry parameters are the aspect ratio (parameter related to the varying radius of the cross section across the croissant axis), the half-angle (the angle between the axis of the leg and the face-on axis of the croissant) and the height. In Figure 5b the best fit of the GCS reconstruction is shown, where it can be seen that the CME is directed south of the equatorial plane and slightly to the west with respect to the Sun-Earth line. It is heavily tilted and therefore in the equatorial plane has a relatively small cross-section and width (small aspect ratio and half angle).

Based on the GCS reconstruction we derive that the CME is Earth-directed with the apex slightly deflected southwest from the Sun-Earth line (Figure 6a). In order to test our CME-ICME association we use the Drag-Based Model (DBM; Vršnak et al. 2013) for heliospheric propagation of ICMEs, which uses 2D CME cone geometry where the leading edge is initially a semicircle, spanning over the full angular width of the CME and flattens as it evolves in time (Žic et al. 2015; Dumbović et al. 2018). As an input we use CME properties obtained by GCS. To obtain the initial kinematical properties of the CME, GCS reconstruction is performed on a series of coronagraph images 2014 May 25, 20:08 – 22:24 UT, where the DBM initial height, time and velocity is given by the last GCS kinematical measurement ($R_0 = 21.9 R_\odot$ at 22:24, $v_0 = 355 \text{ km s}^{-1}$). The width of the cone in the equatorial plane was estimated using $\omega_{\max} - (\omega_{\max} - \omega_{\min}) \times \text{tilt}/90$, where ω_{\max} and ω_{\min} are the maximum and minimum possible widths (face-on and edge-on widths according to Thernisien 2011), and the tilt is the angle of the croissant axis with respect to the equatorial plane. The estimated CME width in the equatorial plane is found to be $\omega = 20^\circ$. Based on the *in situ* measured plasma speed (Figure 5a) we estimate that the ambient solar wind speed is $w \approx 330 \text{ km s}^{-1}$ and we treat the drag parameter γ as a free parameter of the DBM to obtain the most likely arrival time and speed roughly in agreement with the observed arrival time 2014 May 30 12:00 UT and arrival speed $v = 350 \text{ km s}^{-1}$. The best fit is obtained for $\gamma \approx 0.5 \times 10^{-7} \text{ km}^{-1}$. This is a quite high value and indicates a relatively dense and slow solar wind, and low CME mass (see e.g. Vršnak et al. 2013, for details), roughly in agreement with *in situ* and white-light observation of solar wind and CME, respectively.

Next we use GCS results to obtain the FR initial radius. For that purpose we calculate the radius of the croissant cross-section in the direction of the Earth, using formalism described by Thernisien (2011) (the direction of Earth in the croissant face-on system was found to be 16° from the apex). We obtain $a_0 = 3.5 R_\odot$ at the start distance of

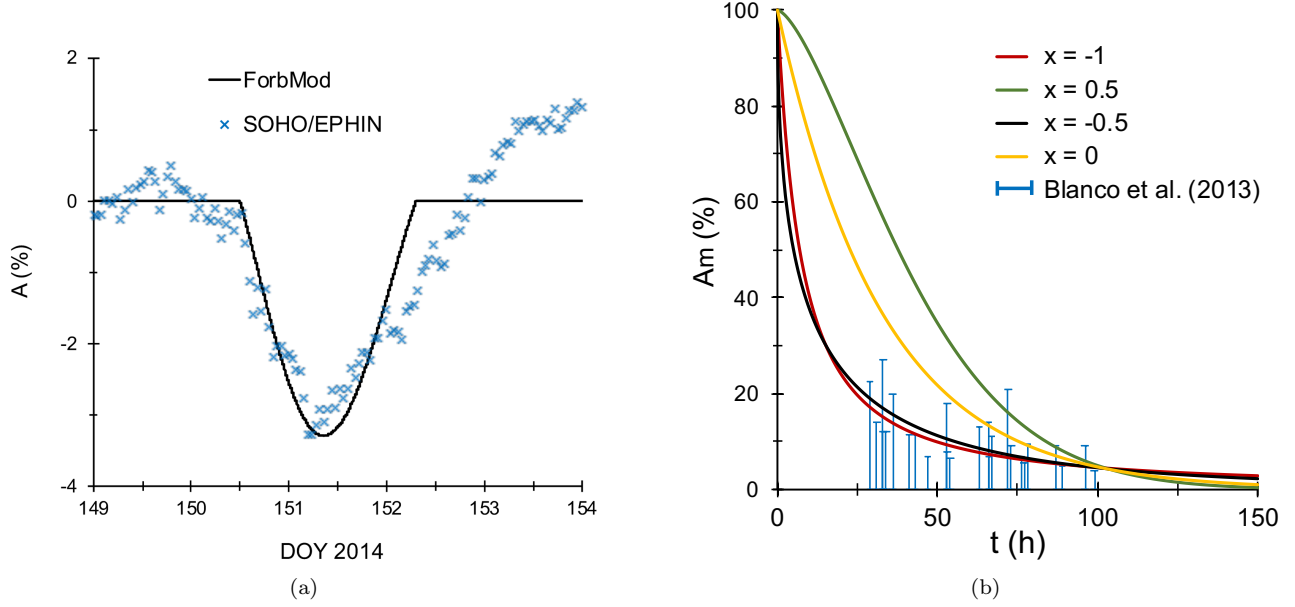


Figure 7. a) *ForbMod* results (black line) for the “best fit” value of the diffusion coefficient near Earth ($D_E = 1.22, 0.55, 0.68$, and 0.45 in $10^{19} \text{ cm}^2 \text{ s}^{-1}$ for $x = 0, 0.5, -0.5$, and -1 , respectively) against FD observation with *SOHO/EPHIN* (blue crosses) for the event 2014 May 30. FD profile is converted from radial dependence into time dependence based on the ICME speed. The start and end of *ForbMod* FD (black line) correspond to the shaded area in Figure 5a. b) *ForbMod* time evolution of the FD magnitude for the event 2014 May 30 for different types of expansion *vs.* observation (data points presented by vertical lines are taken from Figure 8 in Blanco et al. 2013, for explanation see main text).

$R_0 = 18.2 R_\odot$ and the corresponding transit time from R_0 to Earth (*i.e.* diffusion time) is $t = 111.3$ h. We treat the diffusion coefficient at Earth as a free parameter and search for the “best fit”, where the depression in the center of the FR (*i.e.* the FD magnitude) is equal to the measured FD magnitude $A = (3.3 \pm 0.1)\%$. Since all expansion cases show qualitatively the same results (Figure 3a), the best fit curve to the observed FD magnitude is identical for all expansion cases, however, with different corresponding values of the diffusion coefficient near Earth, D_E (Figure 7a). It can be seen in Figure 7a that the observed FD profile is generally described well by *ForbMod*, however there is a slight deviation at the rear of the FR, which could indicate deviation from the circular cross section. Considering the fact that the *in situ* measurements show an asymmetric magnetic field profile with a declining magnetic field strength (first two panels in Figure 5a), one could imagine a slightly deformed FR which should be in such a case somewhat squeezed at the frontal side of the disturbance.

The calculated temporal variation of the FD magnitude depends on the expansion case (Figure 7b), due to different D_E , as is expected from the analysis presented in Figure 3. To check whether the time evolution of the FD magnitude for the 2014 May 30 CME is quantitatively realistic, we compare it to the results of the statistical study by Blanco et al. (2013). In their statistical study, Blanco et al. (2013) used spacecraft measurements from a Sapphire Cherenkov detector onboard *Helios 1* and *Helios 2*, that is mainly sensitive to ~ 1 GV particles, comparable to the response of the *SOHO/EPHIN* (Kühl et al. 2015). Blanco et al. (2013) related the decrease in the C-detector (FD magnitude) versus the time of flight of the CME for a sample of ICMEs detected at *Helios 1* and *Helios 2*. We can use this statistical study to estimate whether the expected time evolution is quantitatively realistic. It should be noted that Blanco et al. (2013) did not measure the FR part of the FD amplitude separately from the shock/sheath part, but present only the total FD amplitude. Therefore, in Figure 7 we represent their measurements with error bars, where the value zero corresponds to no contribution from the FR part to the total FD amplitude, whereas the highest value corresponds to cases where the total FD amplitude is caused solely by the FR. It can be seen in Figure 7b that the time-evolution curve goes through at least some part of those presented Blanco et al. (2013) measurements. However, a more detailed statistical analysis is needed for a more conclusive quantitative analysis, using only the FR part of the total FD amplitude. Nevertheless, we would still expect a significant scatter due to different events with different

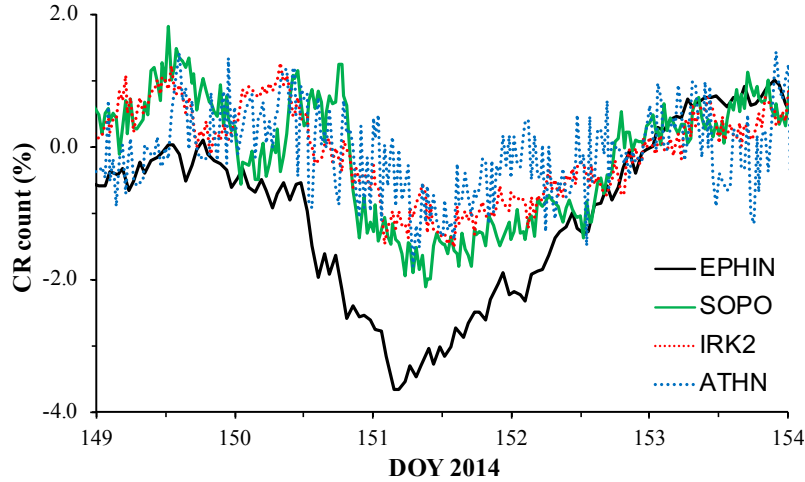


Figure 8. 1-hour *SOHO*/EPHIN and 30-minute neutron monitor relative cosmic ray counts during the 2014 May 30 FD. Neutron monitor measurements (provided by the Neutron Monitor Data Base, NMDB, <http://www.nmdb.eu/>) are corrected for pressure and efficiency, and correspond to different cutoff rigidity: SOPO=South Pole ($P = 0.10$ GV, altitude = 2820 m), IRK2=Irkustk2 ($P = 3.64$ GV, altitude = 2000 m), ATHN=Athens ($P = 8.53$ GV, altitude = 260 m).

expansion characteristics. The time evolution for a specific expansion type could be *e.g.* tested on an event detected at two different times, *i.e.* radially aligned spacecraft at different heliospheric distances.

Finally, we estimate whether the values of D_E are quantitatively realistic. We can see that D_E is around $\sim 10^{19} \text{ cm}^2 \text{ s}^{-1}$, roughly in agreement with Cane et al. (1995) and values obtained from the typical empirical expression used in numerical models (Potgieter 2013). Furthermore, we determine the limit value of the D_E after which FD magnitude at Earth is 0 for all expansion cases, and we find that the critical value is $D_L \approx 3 \times 10^{19} \text{ cm}^2 \text{ s}^{-1}$. According to Equations 23 and 24 by Potgieter (2013) for a magnetic field of $B \approx 12$ nT this would roughly correspond to particle rigidity of $P_L \approx 3$ GV, where P_L can be regarded as an upper limit value of the rigidity where an FD is expected to be observed. Therefore, neutron monitors of different rigidity cutoffs offer convenient means to test this estimation. In Figure 8 it can be seen that a small effect is observed in all selected neutron monitors, although the effect is almost indistinguishable due to daily variations, which are typically of the order of $\approx 1\%$ (Parker 1964; Tiwari et al. 2012). We note that although SOPO has a very low geomagnetic cutoff ($P = 0.1$ GV), we rather expect it to respond to particles $P > 1$ GV, due to atmospheric cutoff (see *e.g.* Clem and Dorman 2000; Moraal et al. 2000, and references therein). IRK2 and ATHN respond roughly to particles of $P > 3.5$ GV and $P > 8.53$ GV, respectively, where no effect is expected, but a small effect is however observed. This could be related to the fact that adiabatic cooling was not taken into account. On the other hand, it might also indicate that the rigidity dependence of the perpendicular diffusion coefficient might be different to the parallel one, as opposed to the *ad hoc* assumption that D_{\perp} scales with D_{\parallel} , used in our calculation of P_L , based on Equations 23 and 24 by Potgieter (2013). In either case, a reliable conclusion would require a more comprehensive analysis which is beyond the scope of this study.

5. CONCLUSION

The presented analytical diffusion–expansion Forbush decrease (FD) model *ForbMod* relies on well established CME observations such as enhanced magnetic field and expansion. The model qualitatively reproduces well the established FD observations of roughly symmetrical FD profile and amplitude progressively decreasing with CME transit time. Quantitatively the model is determined by a complex interplay of the diffusion and expansion depending on the initial conditions (CME radius and diffusion coefficient), as well as the CME expansion type, *i.e.* competing between the decrease of the magnetic field strength and the increase of the cross sectional area.

Several simplifications were used in order to model FDs analytically. We assume constant CME velocity and self similar expansion (no change in the shape) which can be relatively easily justified for slower CMEs but might be an important factor for very fast CMEs. In addition, we assume that the GCR density outside of the FR is constant, *i.e.* that the change of the outside density of $\approx 3\%$ throughout the evolution of the FR to 1 AU will not notably influence the filling rate of GCRs into the FR. We provide an estimate which justifies this assumption and furthermore, with

the same estimates we can justify the applicability of the model to simulate the FR part of two-step FDs. Finally, we assume that GCRs enter the FR only *via* diffusion and neglect possible contributions from adiabatic cooling due to expansion or additional outflow/inflow due to magnetic reconnection. Nevertheless, despite these simplifications used, the model reproduces a number of FD observational properties and furthermore is able to explain the FD observed on 2014 May 30. The observed FD was fitted quite well by *ForbMod* for all expansion types using only the diffusion coefficient as a free parameter, where the diffusion parameter was found to be in the expected range of values.

We conclude that in general the model is able to explain the global properties of FD caused by FR, although there are indications of possible small deviations due to local properties and/or simplifications. These should be the subject of further studies, *e.g.* a statistical study using constrains on the expansion type by *in situ* measurements and/or FR forward modelling. Further testing of the model should also include multi-spacecraft FD measurements. Nevertheless, we note that even in the current form *ForbMod* can be used to better understand the underlying physics in case studies.

The research leading to these results has received funding from the European Union’s Horizon 2020 research and innovation programme under the Marie Skłodowska-Curie grant agreement No 745782. B. V. and M. D. acknowledge financial support by the Croatian Science Foundation under project 6212 “Solar and Stellar Variability”. M.T. acknowledges the support by the FFG/ASAP Programme under grant no. 859729 (SWAMI) and from the Austrian Science Fund (FWF): V195-N16.

REFERENCES

- M. V. Alania, A. Wawrzynczak, V. E. Sdobnov, and M. V. Kravtsova. Temporal Changes in the Rigidity Spectrum of Forbush Decreases Based on Neutron Monitor Data. *Sol. Phys.*, 286:561–576, September 2013. doi:10.1007/s11207-013-0273-0.
- K. P. Arunbabu, H. M. Antia, S. R. Dugad, S. K. Gupta, Y. Hayashi, S. Kawakami, P. K. Mohanty, T. Nonaka, A. Oshima, and P. Subramanian. High-rigidity Forbush decreases: due to CMEs or shocks? *Astron. Astrophys.*, 555:A139, July 2013. doi:10.1051/0004-6361/201220830.
- Badruddin and A. Kumar. Study of the Cosmic-Ray Modulation During the Passage of ICMEs and CIRs. *Sol. Phys.*, 291:559–580, February 2016. doi:10.1007/s11207-015-0843-4.
- L. R. Barnden. The Large-Scale Magnetic Field Configuration Associated With Forbush Decreases. In *Int. Cosmic Ray Conf.*, volume 2 of *International Cosmic Ray Conference*, pages 1277–+, 1973.
- A. Belov, A. Abunin, M. Abunina, E. Eroshenko, V. Oleneva, V. Yanke, A. Papaioannou, and H. Mavromichalaki. Galactic Cosmic Ray Density Variations in Magnetic Clouds. *Sol. Phys.*, 290: 1429–1444, May 2015. doi:10.1007/s11207-015-0678-z.
- A. V. Belov. Forbush effects and their connection with solar, interplanetary and geomagnetic phenomena. In N. Gopalswamy and D. F. Webb, editors, *IAU Symp.*, volume 257 of *IAU Symp.*, pages 439–450, March 2009. doi:10.1017/S1743921309029676.
- J. J. Blanco, M. A. Hidalgo, R. Gómez-Herrero, J. Rodríguez-Pacheco, B. Heber, R. F. Wimmer-Schweingruber, and C. Martín. Energetic-particle-flux decreases related to magnetic cloud passages as observed by the Helios 1 and 2 spacecraft. *Astron. Astrophys.*, 556:A146, August 2013. doi:10.1051/0004-6361/201321739.
- V. Bothmer and R. Schwenn. The structure and origin of magnetic clouds in the solar wind. *Ann. Geophys.*, 16: 1–24, January 1998. doi:10.1007/s00585-997-0001-x.
- G. E. Brueckner, R. A. Howard, M. J. Koomen, C. M. Korendyke, D. J. Michels, J. D. Moses, D. G. Socker, K. P. Dere, P. L. Lamy, A. Llebaria, M. V. Bout, R. Schwenn, G. M. Simnett, D. K. Bedford, and C. J. Eyles. The Large Angle Spectroscopic Coronagraph (LASCO). *Sol. Phys.*, 162:357–402, December 1995. doi:10.1007/BF00733434.
- L. Burlaga, E. Sittler, F. Mariani, and R. Schwenn. Magnetic loop behind an interplanetary shock - Voyager, Helios, and IMP 8 observations. *J. Geophys. Res.*, 86: 6673–6684, August 1981. doi:10.1029/JA086iA08p06673.
- E. Butkov. *Mathematical Physics*. Addison-Wesley Publishing Company, Reading, Massachusetts, 1968.
- H. V. Cane. Cosmic ray decreases and magnetic clouds. *J. Geophys. Res.*, 98:3509–3512, March 1993. doi:10.1029/92JA02479.
- H. V. Cane. Coronal Mass Ejections and Forbush Decreases. *Space Sci. Rev.*, 93:55–77, July 2000. doi:10.1023/A:1026532125747.
- H. V. Cane, I. G. Richardson, T. T. von Rosenvinge, and G. Wibberenz. Cosmic ray decreases and shock structure: A multispacecraft study. *J. Geophys. Res.*, 99: 21429, November 1994. doi:10.1029/94JA01529.
- H. V. Cane, I. G. Richardson, and G. Wibberenz. The Response of Energetic Particles to the Presence of Ejecta Material. *Int. Cosmic Ray Conf.*, 4:377, 1995.
- P. J. Cargill, J. Chen, D. S. Spicer, and S. T. Zalesak. The deformation of flux tubes in the solar wind with applications to the structure of magnetic clouds and CMEs. In J. J. Hunt, editor, *Solar Dynamic Phenomena and Solar Wind Consequences, the Third SOHO Workshop*, volume 373 of *ESA Special Publication*, page 291, December 1994.
- J. M. Clem and L. I. Dorman. Neutron Monitor Response Functions. *Space Sci. Rev.*, 93:335–359, July 2000. doi:10.1023/A:1026508915269.
- J. Crank. *The Mathematics of Diffusion, 2nd Edition*. Oxford University Press, London, 1975.
- S. Dasso, M. S. Nakwacki, P. Démoulin, and C. H. Mandrini. Progressive Transformation of a Flux Rope to an ICME. Comparative Analysis Using the Direct and Fitted Expansion Methods. *Sol. Phys.*, 244:115–137, August 2007. doi:10.1007/s11207-007-9034-2.
- P. Démoulin, M. S. Nakwacki, S. Dasso, and C. H. Mandrini. Expected in Situ Velocities from a Hierarchical Model for Expanding Interplanetary Coronal Mass Ejections. *Sol. Phys.*, 250:347–374, August 2008. doi:10.1007/s11207-008-9221-9.
- V. Domingo, B. Fleck, and A. I. Poland. The SOHO Mission: an Overview. *Sol. Phys.*, 162:1–37, December 1995. doi:10.1007/BF00733425.
- M. Dumbović, B. Vršnak, J. Čalogović, and M. Karlica. Cosmic ray modulation by solar wind disturbances. *Astron. Astrophys.*, 531:A91+, July 2011. doi:10.1051/0004-6361/201016006.
- M. Dumbović, B. Vršnak, J. Čalogović, and R. Župan. Cosmic ray modulation by different types of solar wind disturbances. *Astron. Astrophys.*, 538:A28, February 2012. doi:10.1051/0004-6361/201117710.

- M. Dumbović, J. Čalogović, B. Vršnak, M. Temmer, M. L. Mays, A. Veronig, and I. Piantischtsch. The Drag-based Ensemble Model (DBEM) for Coronal Mass Ejection Propagation. *Astrophys. J.*, 854:180, February 2018. doi:10.3847/1538-4357/aaaa66.
- S. E. Forbush. On the effects in cosmic-ray intensity observed during the recent magnetic storm. *Phys. Rev.*, 51(12):1108–1109, Jun 1937. doi:10.1103/PhysRev.51.1108.3.
- J. Gieseler and B. Heber. Spatial gradients of GCR protons in the inner heliosphere derived from Ulysses COSPIN/KET and PAMELA measurements. *Astron. Astrophys.*, 589:A32, May 2016. doi:10.1051/0004-6361/201527972.
- N. Gopalswamy, A. Lara, R. P. Lepping, M. L. Kaiser, D. Berdichevsky, and O. C. St. Cyr. Interplanetary acceleration of coronal mass ejections. *Geophys. Res. Lett.*, 27:145–148, January 2000. doi:10.1029/1999GL003639.
- A. M. Gulisano, P. Démoulin, S. Dasso, M. E. Ruiz, and E. Marsch. Global and local expansion of magnetic clouds in the inner heliosphere. *Astron. Astrophys.*, 509: A39, January 2010. doi:10.1051/0004-6361/200912375.
- A. M. Gulisano, P. Démoulin, S. Dasso, and L. Rodriguez. Expansion of magnetic clouds in the outer heliosphere. *Astron. Astrophys.*, 543:A107, July 2012. doi:10.1051/0004-6361/201118748.
- B. Heber, C. Wallmann, D. Galsdorf, C. Herbst, P. Kuhl, M. Dumbović, B. Vršnak, A. Veronig, M. Temmer, C. Möstl, and S. Dalla. Forbush decreases associated to Stealth Coronal Mass Ejections. *Cent. European Astrophys. Bull.*, 2015.
- P. Hess and J. Zhang. Stereoscopic Study of the Kinematic Evolution of a Coronal Mass Ejection and Its Driven Shock from the Sun to the Earth and the Prediction of Their Arrival Times. *Astrophys. J.*, 792:49, September 2014. doi:10.1088/0004-637X/792/1/49.
- M. Janvier, P. Démoulin, and S. Dasso. In situ properties of small and large flux ropes in the solar wind. *J. Geophys. Res.*, 119:7088–7107, September 2014. doi:10.1002/2014JA020218.
- J. R. Jokipii. Cosmic-Ray Propagation. I. Charged Particles in a Random Magnetic Field. *Astrophys. J.*, 146:480, November 1966. doi:10.1086/148912.
- J. R. Jokipii. Propagation of cosmic rays in the solar wind. *Reviews of Geophysics and Space Physics*, 9:27–87, 1971. doi:10.1029/RG009i001p00027.
- A. P. Jordan, H. E. Spence, J. B. Blake, and D. N. A. Shaul. Revisiting two-step Forbush decreases. *J. Geophys. Res.*, 116(A15):A11103, November 2011. doi:10.1029/2011JA016791.
- M. L. Kaiser, T. A. Kucera, J. M. Davila, O. C. St. Cyr, M. Guhathakurta, and E. Christian. The STEREO Mission: An Introduction. *Space Sci. Rev.*, 136:5–16, April 2008. doi:10.1007/s11214-007-9277-0.
- E. Kilpua, H. E. J. Koskinen, and T. I. Pulkkinen. Coronal mass ejections and their sheath regions in interplanetary space. *Living Reviews in Solar Physics*, 14:5, November 2017. doi:10.1007/s41116-017-0009-6.
- M. Kozai, K. Munakata, C. Kato, T. Kuwabara, M. Rockenbach, A. Dal Lago, N. J. Schuch, C. R. Braga, R. R. S. Mendonça, H. K. A. Jassar, M. M. Sharma, M. L. Duldig, J. E. Humble, P. Evenson, I. Sabbah, and M. Tokumaru. Average Spatial Distribution of Cosmic Rays behind the Interplanetary Shock – Global Muon Detector Network Observations. *Astrophys. J.*, 825:100, July 2016. doi:10.3847/0004-637X/825/2/100.
- W. Krittinatham and D. Ruffolo. Drift Orbits of Energetic Particles in an Interplanetary Magnetic Flux Rope. *Astrophys. J.*, 704:831–841, October 2009. doi:10.1088/0004-637X/704/1/831.
- Y. Kubo and H. Shimazu. Effect of Finite Larmor Radius on Cosmic-ray Penetration into an Interplanetary Magnetic Flux Rope. *Astrophys. J.*, 720:853–861, September 2010. doi:10.1088/0004-637X/720/1/853.
- P. Kuhl, S. Banjac, B. Heber, J. Labrenz, R. Müller-Mellin, and C. Terasa. Extended Measurement Capabilities of the Electron Proton Helium INstrument aboard SOHO - Understanding single detector count rates. *Cent. European Astrophys. Bull.*, 39:119–124, 2015.
- T. Kuwabara, J. W. Bieber, P. Evenson, K. Munakata, S. Yasue, C. Kato, A. Fushishita, M. Tokumaru, M. L. Duldig, J. E. Humble, M. R. Silva, A. Dal Lago, and N. J. Schuch. Determination of interplanetary coronal mass ejection geometry and orientation from ground-based observations of galactic cosmic rays. *J. Geophys. Res.*, 114(A13):A05109, May 2009. doi:10.1029/2008JA013717.
- H. Laster, A. M. Lenchek, and S. F. Singer. Forbush Decreases Produced by Diffusive Deceleration Mechanism in Interplanetary Space. *J. Geophys. Res.*, 67:2639–2643, July 1962. doi:10.1029/JZ067i007p02639.
- D. J. Lawrence, P. N. Peplowski, W. C. Feldman, N. A. Schwadron, and H. E. Spence. Galactic cosmic ray variations in the inner heliosphere from solar distances less than 0.5 AU: Measurements from the MESSENGER Neutron Spectrometer. *J. Geophys. Res.*, 121:7398–7406, August 2016. doi:10.1002/2016JA022962.

- J. A. Le Roux and M. S. Potgieter. The simulation of Forbush decreases with time-dependent cosmic-ray modulation models of varying complexity. *Astron. Astrophys.*, 243:531–545, March 1991.
- M. Leitner, C. J. Farrugia, C. Möstl, K. W. Ogilvie, A. B. Galvin, R. Schwenn, and H. K. Biernat. Consequences of the force-free model of magnetic clouds for their heliospheric evolution. *J. Geophys. Res.*, 112:A06113, June 2007. doi:10.1029/2006JA011940.
- J. R. Lemen, A. M. Title, D. J. Akin, P. F. Boerner, C. Chou, J. F. Drake, D. W. Duncan, C. G. Edwards, F. M. Friedlaender, G. F. Heyman, N. E. Hurlburt, N. L. Katz, G. D. Kushner, M. Levay, R. W. Lindgren, D. P. Mathur, E. L. McFeaters, S. Mitchell, R. A. Rehse, C. J. Schrijver, L. A. Springer, R. A. Stern, T. D. Tarbell, J.-P. Wuelser, C. J. Wolfson, C. Yanari, J. A. Bookbinder, P. N. Cheimets, D. Caldwell, E. E. Deluca, R. Gates, L. Golub, S. Park, W. A. Podgorski, R. I. Bush, P. H. Scherrer, M. A. Gummin, P. Smith, G. Auken, P. Jerram, P. Pool, R. Soufli, D. L. Windt, S. Beardsley, M. Clapp, J. Lang, and N. Waltham. The Atmospheric Imaging Assembly (AIA) on the Solar Dynamics Observatory (SDO). *Sol. Phys.*, 275:17–40, January 2012. doi:10.1007/s11207-011-9776-8.
- R. P. Lepping, L. F. Burlaga, and J. A. Jones. Magnetic field structure of interplanetary magnetic clouds at 1 AU. *J. Geophys. Res.*, 95:11957–11965, August 1990. doi:10.1029/JA095iA08p11957.
- R. P. Lepping, M. H. Acuña, L. F. Burlaga, W. M. Farrell, J. A. Slavin, K. H. Schatten, F. Mariani, N. F. Ness, F. M. Neubauer, Y. C. Whang, J. B. Byrnes, R. S. Kennon, P. V. Panetta, J. Scheifele, and E. M. Worley. The Wind Magnetic Field Investigation. *Space Sci. Rev.*, 71:207–229, February 1995. doi:10.1007/BF00751330.
- Y. Liu, J. D. Richardson, J. W. Belcher, C. Wang, Q. Hu, and J. C. Kasper. Constraints on the global structure of magnetic clouds: Transverse size and curvature. *J. Geophys. Res.*, 111(A10):A12S03, December 2006. doi:10.1029/2006JA011890.
- John A. Lockwood. Forbush decreases in the cosmic radiation. *Space Sci. Rev.*, 12:658–715, 1971. ISSN 0038-6308. URL <http://dx.doi.org/10.1007/BF00173346>. doi:10.1007/BF00173346.
- S. Lundquist. On the Stability of Magneto-Hydrostatic Fields. *Physical Review*, 83:307–311, July 1951. doi:10.1103/PhysRev.83.307.
- W. Manchester, E. K. J. Kilpua, Y. D. Liu, N. Lugaz, P. Riley, T. Török, and B. Vršnak. The Physical Processes of CME/ICME Evolution. *Space Sci. Rev.*, 212:1159–1219, November 2017. doi:10.1007/s11214-017-0394-0.
- W. B. Manchester, IV, B. van der Holst, and B. Lavraud. Flux rope evolution in interplanetary coronal mass ejections: the 13 May 2005 event. *Plasma Physics and Controlled Fusion*, 56(6):064006, June 2014. doi:10.1088/0741-3335/56/6/064006.
- J. Marquardt, B. Heber, M. S. Potgieter, and R. D. Strauss. Energy spectra of carbon and oxygen with HELIOS E6. Radial gradients of anomalous cosmic ray oxygen within 1 AU. *Astron. Astrophys.*, 610:A42, February 2018. doi:10.1051/0004-6361/201731490.
- J. J. Masías-Meza, S. Dasso, P. Démoulin, L. Rodriguez, and M. Janvier. Superposed epoch study of ICME sub-structures near Earth and their effects on Galactic cosmic rays. *Astron. Astrophys.*, 592:A118, August 2016. doi:10.1051/0004-6361/201628571.
- H. Moraal, A. Belov, and J. M. Clem. Design and co-Ordination of Multi-Station International Neutron Monitor Networks. *Space Sci. Rev.*, 93:285–303, July 2000. doi:10.1023/A:1026504814360.
- P. Morrison. Solar Origin of Cosmic-Ray Time Variations. *Phys. Rev.*, 101:1397–1404, February 1956. doi:10.1103/PhysRev.101.1397.
- R. Müller-Mellin, H. Kunow, V. Fleißner, E. Pehlke, E. Rode, N. Röschmann, C. Scharnberg, H. Sierks, P. Rusznyak, S. McKenna-Lawlor, I. Elenndt, J. Sequeiros, D. Meziat, S. Sanchez, J. Medina, L. Del Peral, M. Witte, R. Marsden, and J. Henrion. COSTEP - Comprehensive Suprathermal and Energetic Particle Analyser. *Sol. Phys.*, 162:483–504, December 1995. doi:10.1007/BF00733437.
- K. Munakata, S. Yasue, C. Kato, J. Kota, M. Tokumaru, M. Kojima, A. A. Darwish, T. Kuwabara, and J. W. Bieber. On the Cross-Field Diffusion of Galactic Cosmic Rays into an ICME. *Advances in Geosciences, Volume 2: Solar Terrestrial (ST)*, 2:115, 2006. doi:10.1142/9789812707185_0009.
- K. W. Ogilvie, D. J. Chornay, R. J. Fritzenreiter, F. Hunsaker, J. Keller, J. Lobell, G. Miller, J. D. Scudder, E. C. Sittler, Jr., R. B. Torbert, D. Bodet, G. Needell, A. J. Lazarus, J. T. Steinberg, J. H. Tappan, A. Mavretic, and E. Gergin. SWE, A Comprehensive Plasma Instrument for the Wind Spacecraft. *Space Sci. Rev.*, 71:55–77, February 1995. doi:10.1007/BF00751326.

- E. N. Parker. Theory of streaming of cosmic rays and the diurnal variation. *Planet. Space. Sci.*, 12:735–749, August 1964. doi:10.1016/0032-0633(64)90054-6.
- E. N. Parker. The passage of energetic charged particles through interplanetary space. *Planet. Space. Sci.*, 13: 9–+, January 1965. doi:10.1016/0032-0633(65)90131-5.
- M. S. Potgieter. Solar Modulation of Cosmic Rays. *Living Reviews in Solar Physics*, 10:3, June 2013. doi:10.12942/lrsp-2013-3.
- J. J. Quenby, T. Mulligan, J. B. Blake, J. E. Mazur, and D. Shaul. Local and nonlocal geometry of interplanetary coronal mass ejections: Galactic cosmic ray (GCR) short-period variations and magnetic field modeling. *J. Geophys. Res.*, 113(A12):A10102, October 2008. doi:10.1029/2007JA012849.
- I. G. Richardson and H. V. Cane. Galactic Cosmic Ray Intensity Response to Interplanetary Coronal Mass Ejections/Magnetic Clouds in 1995 - 2009. *Sol. Phys.*, 270:609–627, June 2011. doi:10.1007/s11207-011-9774-x.
- A. P. Rouillard. Relating white light and in situ observations of coronal mass ejections: A review. *J. Atmos. Sol. Terr. Phys.*, 73:1201–1213, June 2011. doi:10.1016/j.jastp.2010.08.015.
- A. Ruffenach, B. Lavraud, C. J. Farrugia, P. Démoulin, S. Dasso, M. J. Owens, J.-A. Sauvaud, A. P. Rouillard, A. Lynnyk, C. Foullon, N. P. Savani, J. G. Luhmann, and A. B. Galvin. Statistical study of magnetic cloud erosion by magnetic reconnection. *J. Geophys. Res.*, 120:43–60, January 2015. doi:10.1002/2014JA020628.
- D. Ruffolo, P. Chuychai, P. Wongpan, J. Minnie, J. W. Bieber, and W. H. Matthaeus. Perpendicular Transport of Energetic Charged Particles in Nonaxisymmetric Two-Component Magnetic Turbulence. *Astrophys. J.*, 686:1231–1244, October 2008. doi:10.1086/591493.
- N. Sachdeva, P. Subramanian, R. Colaninno, and A. Vourlidas. CME Propagation: Where does Aerodynamic Drag 'Take Over'? *Astrophys. J.*, 809:158, August 2015. doi:10.1088/0004-637X/809/2/158.
- N. R. Sheeley, J. H. Walters, Y.-M. Wang, and R. A. Howard. Continuous tracking of coronal outflows: Two kinds of coronal mass ejections. *J. Geophys. Res.*, 104: 24739–24768, November 1999. doi:10.1029/1999JA900308.
- S. F. Singer, A. M. Lenchek, and H. Laster. Forbush Decreases Produced by Diffusive Deceleration Mechanism in Interplanetary Space. *Journal of the Physical Society of Japan Supplement*, 17:583, 1962.
- P. Subramanian, H. M. Antia, S. R. Dugad, U. D. Goswami, S. K. Gupta, Y. Hayashi, N. Ito, S. Kawakami, H. Kojima, P. K. Mohanty, P. K. Nayak, T. Nonaka, A. Oshima, K. Sivaprasad, H. Tanaka, S. C. Tonwar, and The Grapes-3 Collaboration. Forbush decreases and turbulence levels at coronal mass ejection fronts. *Astron. Astrophys.*, 494:1107–1118, February 2009. doi:10.1051/0004-6361:200809551.
- A. Thernisien. Implementation of the Graduated Cylindrical Shell Model for the Three-dimensional Reconstruction of Coronal Mass Ejections. *Astrophys. J. Suppl.*, 194:33, June 2011. doi:10.1088/0067-0049/194/2/33.
- A. Thernisien, A. Vourlidas, and R. A. Howard. Forward Modeling of Coronal Mass Ejections Using STEREO/SECCHI Data. *Sol. Phys.*, 256:111–130, May 2009. doi:10.1007/s11207-009-9346-5.
- A. F. R. Thernisien, R. A. Howard, and A. Vourlidas. Modeling of Flux Rope Coronal Mass Ejections. *Astrophys. J.*, 652:763–773, November 2006. doi:10.1086/508254.
- A. K. Tiwari, A. Singh, and S. P. Agrawal. Study of the Diurnal Variation of Cosmic Rays during Different Phases of Solar Activity. *Sol. Phys.*, 279:253–267, July 2012. doi:10.1007/s11207-012-9962-3.
- B. Vršnak, T. Žic, D. Vrbanc, M. Temmer, T. Rollett, C. Möstl, A. Veronig, J. Čalogović, M. Dumbović, S. Lulić, Y.-J. Moon, and A. Shanmugaraju. Propagation of Interplanetary Coronal Mass Ejections: The Drag-Based Model. *Sol. Phys.*, 285:295–315, July 2013. doi:10.1007/s11207-012-0035-4.
- A. Wawrzynczak and M. V. Alania. Modeling and data analysis of a Forbush decrease. *Adv. Space Res.*, 45: 622–631, March 2010. doi:10.1016/j.asr.2009.09.005.
- W. R. Webber and J. A. Lockwood. A new look at the <70 MeV cosmic ray radial gradients in the heliosphere measured by spacecraft. *J. Geophys. Res.*, 104: 2487–2498, February 1999. doi:10.1029/1998JA900058.
- G. Wibberenz, J. A. Le Roux, M. S. Potgieter, and J. W. Bieber. Transient Effects and Disturbed Conditions. *Space Sci. Rev.*, 83:309–348, January 1998.
- T. H. Zurbuchen and I. G. Richardson. In-Situ Solar Wind and Magnetic Field Signatures of Interplanetary Coronal Mass Ejections. *Space Sci. Rev.*, 123:31–43, March 2006. doi:10.1007/s11214-006-9010-4.
- T. Žic, B. Vršnak, and M. Temmer. Heliospheric Propagation of Coronal Mass Ejections: Drag-based Model Fitting. *Astrophys. J. Suppl.*, 218:32, June 2015. doi:10.1088/0067-0049/218/2/32.